Journal of Materials Chemistry A

PAPER

View Article Online
View Journal | View Issue

Cite this: J. Mater. Chem. A, 2019, 7, 827

Energy level engineering in transition-metal doped spinel-structured nanosheets for efficient overall water splitting†

Feili Lai,[ab] Jianrui Feng,[a] Xiaobin Ye,[b] Wei Zong,[a] Guanjie He,[c] Yue-E Miao,*[a] Xuemei Han,[d] Xing Yi Ling,[d] Ivan P. Parkin,[c] Bicai Pan,[b] Yongfu Sun*[b] and Tianxi Liu*[a]

Received 22nd October 2018
Accepted 3rd December 2018

DOI: 10.1039/c8ta10162k

rsc.li/materials-a

Unraveling the role of transition-metal doping in affecting the native spinel-structured nanosheets' water splitting remains a grand challenge. In this work, a series of spinel-structured nanosheets wrapped hollow nitrogen-doped carbon polyhedrons were constructed, and doped transition-metal domains were deliberately introduced on the surface. Theoretical investigations show that their energy level can be finely tuned *via* direct transition-metal doping engineering. As a prototype, an Fe-doped $NiCo_2O_4$ nanosheets wrapped hollow nitrogen-doped carbon polyhedron (Fe–$NiCo_2O_4$@HNCP) exhibits outstanding bifunctional electrocatalytic performances with low overpotentials (η = 270 mV for OER, η = 84 mV for HER), low Tafel slopes (b = 42 mV dec^{-1} for OER, b = 47 mV dec^{-1} for HER), and high durability. The enhanced performance is attributed to the synergistic effects of energy level matching for electron transfer, and partial charge delocalization-induced rich active sites for reactant adsorption *via* thermodynamic and kinetic acceleration. This work may open a new pathway to design highly active and stable transition-metal doped electrocatalysts by manipulated energy levels for efficient overall water splitting.

Introduction

Water electrolysis has been regarded as a promising approach to split water into molecular hydrogen (H_2), a clean energy carrier for both stationary power and transportation.[1–4] To expedite the kinetics of water electrolysis, advanced electrocatalysts are always needed to minimize the overpotentials for both hydrogen evolution and oxygen evolution reactions (HER and OER).[5–9] To date, platinum-group metals and noble metal oxides (such as iridium oxide and ruthenium oxide) display unbeatable electrocatalytic activity to drive the HER and OER.[10,11] However, the scarcity and high cost of precious noble metals make it necessary to search for low-cost ideal replacements with low overpotential, small Tafel slope and high exchange current density for sustainable electrocatalysis.[12]

Recently, metal oxides (MO_x; M = Ni, Co, Zn, Cu, Fe, Mn) as electrocatalysts have attracted great interest for water splitting due to their efficient adsorption towards reaction intermediates.[13–15] To break their confined sluggish kinetics for water splitting, the nanostructure and composition of MO_x-based catalysts should be optimized to expose the largest extent active sites. For example, an abundance of novel nanostructures have been put forward, such as Co_3O_4/$NiCo_2O_4$ double-shelled nanocages,[16] hierarchical $NiCo_2O_4$ hollow microcuboids,[17] cobalt(II) oxide nanorods,[18] and ultrathin spinel-structured nanosheets.[19] All these well-structured materials display extraordinary electrocatalytic activity for water splitting. Unfortunately, nanostructured MO_x composites still suffer from poor thermodynamic processes due to their large bandgap and low electrical conductivity, thus attracting other ways to modulate their electrocatalytic properties. Learning from the transition-metal centered protein matrix of enzymes in nature, some functional artificial analogues, such as transition-metal doped metallic oxides/sulfide/carbide and single atom dispersed systems, have been prepared, which also show modified electronic density around the doped centers.[20,21] Therefore, it may be an efficient strategy to meet the reaction

[a]State Key Laboratory for Modification of Chemical Fibers and Polymer Materials, College of Materials Science and Engineering, Innovation Center for Textile Science and Technology, Donghua University, Shanghai 201620, P. R. China. E-mail: txliu@dhu.edu.cn; yuee_miao@dhu.edu.cn

[b]Hefei National Laboratory for Physical Science at the Microscale, University of Science and Technology of China, Hefei, Anhui 230026, P. R. China. E-mail: yfsun@ustc.edu.cn

[c]Christopher Ingold Laboratory, Department of Chemistry, University College London, 20 Gordon Street, London WC1H 0AJ, UK

[d]Division of Chemistry and Biological Chemistry, School of Physical and Mathematical Sciences, Nanyang Technological University, 21 Nanyang Link, Singapore 637371

† Electronic supplementary information (ESI) available: Optimized crystal structures, SEM images, TEM images, schematic illustration, XRD patterns, AFM images, TGA profiles, overpotentials and TOF values, cyclic voltammograms, calculated adsorption energy, charge density distribution, calculated DOS, XPS spectra, polarization curves, Tafel curves, and a comparison of electrocatalytic activities for various catalysts. See DOI: 10.1039/c8ta10162k

conditions required for water splitting by tailoring the energy level of MO_x-based catalysts.

By using $NiCo_2O_4$ as a typical example, the band structures of a series of transition-metal doped $NiCo_2O_4$ (TM-$NiCo_2O_4$) were simulated by density functional theory (DFT) calculations. After the transition-metal doping in pristine $NiCo_2O_4$, the energy levels of TM-$NiCo_2O_4$ were shifted to the appropriate positions with a much lower applied energy/overpotential for the electron transfer, thus indicating that TM-$NiCo_2O_4$ are promising electrocatalysts for OER (Fig. 1). Particularly, here we find that the iron atom (Fe) is the most suitable dopant to modulate the electronic structure of $NiCo_2O_4$ for a better energy level of Fe–$NiCo_2O_4$ (Fig. S1†).

Inspired by the above-mentioned advantages, a series of transition-metal doped $NiCo_2O_4$ nanosheets wrapped hollow N-doped carbon polyhedrons (TM-$NiCo_2O_4$@HNCP, TM = Fe, Zn, Cu, and Mn), were synthesized by using *in situ* polymerization for the synthesis of a polyaniline polyhedron, acid-etching for the removal of the rhombic dodecahedral zeolitic imidazolate framework-67 (ZIF-67) core, and hydrothermal reaction for the uniform dispersion of TM-$NiCo_2O_4$ nanosheets. The doping engineering is beneficial to tailoring the energy levels of $NiCo_2O_4$ nanosheets into lower onset energy levels for electrocatalysis and partially delocalizing the charge around the transition-metal atoms on the very surface of TM-$NiCo_2O_4$. Especially, Fe–$NiCo_2O_4$@NHCP exhibits better electrochemical activity towards water splitting, which is attributed to the 3d electron configuration of the partially delocalized charge in Fe–$NiCo_2O_4$ with increased active sites that interact well between the Fe–$NiCo_2O_4$ nanosheets and HNCP support with an enhanced interfacial charge transfer. Moreover, we have proved that this transition-metal doping engineering could be extended to other spinel-structured nanosheets, thus providing a general strategy for boosting highly efficient water splitting performance.

Experimental

Synthesis of hollow nitrogen-doped carbon polyhedron

20 μL of aniline monomer was added into 100 mL of ZIF-67 dispersion (1 mg mL^{-1}) under sonication. Then, 0.95 g of $(NH_4)_2S_2O_8$ dissolved in 30 mL of deionized water was added, and stirred overnight. The resulting precipitates were washed with deionized water, dried at 60 °C and are denoted as ZIF-67@PANI. For the removal of the ZIF-67 template, ZIF-67@PANI was stirred in HCl solution (1 mol L^{-1}) for 6 h at room temperature, thus obtaining a hollow PANI polyhedron. The hollow PANI polyhedron was placed in a tube furnace, heated to 800 °C with a ramp rate of 5 °C min^{-1}, and kept for 3 h in N_2 flow, to yield hollow nitrogen-doped carbon polyhedron (NHCP).

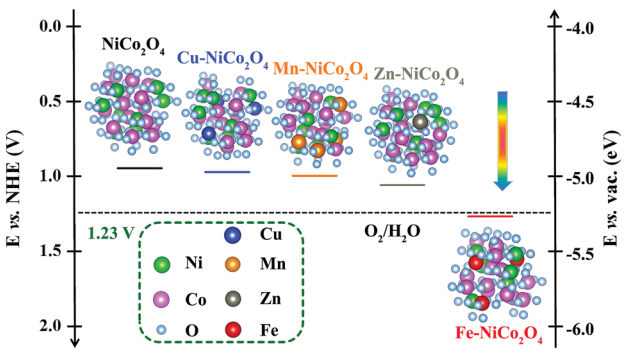

Fig. 1 Calculated band structure diagram for pristine $NiCo_2O_4$, Cu–$NiCo_2O_4$, Mn–$NiCo_2O_4$, Zn–$NiCo_2O_4$, and Fe–$NiCo_2O_4$, compared with OER related energy levels.

Synthesis of transition-metal doped $NiCo_2O_4$@HNCP (TM-$NiCo_2O_4$@HNCP)

For the preparation of different TM-$NiCo_2O_4$@HNCP samples, 110 mg of $Ni(NO_3)_2 \cdot 6H_2O$, 221 mg of $Co(NO_3)_2 \cdot 6H_2O$, and 560 mg of methenamine (HMT) were added into 30 mL of ethanol/water (v/v = 1 : 1) solution with 6×10^{-5} mol of the corresponding metal ions from $FeCl_2$, $Zn(NO_3)_2 \cdot 6H_2O$, $Cu(NO_3)_2$, and $Mn(NO_3)_2$. After sonication for 10 min, 20 mg of HNCP was dispersed into the above clear solution with another 2 h of sonication. The reaction solution was transferred to a 50 mL flask, and then heated in an oil bath at 80 °C for 8 h. The product was collected by centrifugation, washed with deionized water/ethanol, and dried at 60 °C. Then, the powder was annealed in a tubular furnace at 350 °C for 2 h in a N_2 gas atmosphere with a ramp rate of 5 °C min^{-1}. For comparison, $NiCo_2O_4$@HNCP was synthesized using the same steps except for adding the metal salt.

Characterization

The morphology of the hybrids was observed by scanning electron microscopy (SEM, LEO 1550-Gemini) operating at 3 kV. The transmission electron microscopy (TEM) was carried out on a JEM-2100F field emission electron microscope at an acceleration voltage of 200 kV. High-resolution TEM (HRTEM, JEOL ARM 200F) was operated at an acceleration voltage of 200 kV. Atomic force microscopy (AFM) was carried out on the Veeco DI Nano-scope MultiMode V system. X-ray diffraction (XRD) patterns were recorded on a Smartlab X-ray diffractometer (Cu K_α, λ = 0.1541 nm). X-Ray photoelectron spectra (XPS) were acquired by an ESCALAB MK II with Mg K_α as the excitation source. The binding energies obtained in the XPS spectral analysis were corrected for specimen charging by referencing C 1s to 284.8 eV. N_2 physisorption experiments were carried out at −196 °C with 40–60 mg samples on a Quadrasorb apparatus from Quantachrome Instruments. Prior to all the measurements, the samples were outgassed under vacuum at 150 °C for 20 h. Specific surface areas (SSAs) were calculated using the multi-point Brunauer–Emmett–Teller (BET) model (p/p_0 = 0.05–0.2). Total pore volumes (V_t) were determined at p/p_0 = 0.95. SSAs and V_t were calculated from the data obtained by measurements from 40–60 mg of the sample. Pore size distributions were calculated using the quenched-solid density functional theory (QSDFT) method (adsorption branch kernel) for N_2 adsorbed on carbon at −196 °C. Thermogravimetric analysis (TGA) was conducted with a Netzsch TG 209 F1 device

under a constant artificial air flow with a heating rate of 10 °C min^{-1}.

Theoretical calculation details

In this work, simulations were based on density functional theory (DFT). The Vienna ab initio simulation package (VASP) was implemented to optimize the structures and investigate their properties. The ion–electron interactions were depicted by projector augmented waves (PAW)[22] with the function of Perdew, Burke and Ernzerhof (PBE)[23] based on the generalized gradient approximation (GGA), which was adopted to describe the exchange and correlation potential. In this calculation, 5 × 5 × 5 and 5 × 5 × 1 Monkhorst–Pack[24] sampled *k* points were used for the bulk and surface computations and a cut-off energy of 400 eV was adopted. The threshold of convergence was set to 1×10^{-4} eV and 0.05 eV $Å^{-1}$ for the self-consistent field (SCF) and ion steps, respectively. For the d-band center calculation, the integrating section was selected from −3 to 0 eV (*vs.* the Fermi level); however, the region lower than −3 eV gave a negligible contribution as it was too far away from the Fermi level. To build structures of Zn, Fe, Mn and Cu doped $NiCo_2O_4$, the Co and Ni atoms were homogeneously replaced by heteroatoms, according to the experimentally measured composition.

The free energy diagram of HER was calculated by the equation $G = E + ZPE - TS$, where *E*, *ZPE*, *T* and *S* are the DFT derived energy, zero-point energy, temperature in Kelvins and entropy, respectively. For the mechanism in alkaline media, we assumed that it follows a Volmer–Heyrovsky route, in accordance with the experimentally observed Tafel slope.[25] The two stages of hydrogen evolution are listed as the follow equations:

$$* + H_2O + e^- = *H + OH^- \text{ (Volmer stage)} \quad (1)$$

$$*H + H_2O + e^- = * + H_2 + OH^- \text{ (Heyrovsky stage)} \quad (2)$$

The barriers of the Volmer stage were estimated by the nudged elastic band (NEB) method.[26]

Electrochemical measurements

All the electrochemical measurements were carried out on a CHI660B electrochemical workstation (CH Instruments, Inc., Shanghai) with a standard three-electrode system at room temperature (25 °C).[27,28] A glassy carbon electrode (GCE) 4 mm in diameter was used as the support for the catalysts. In brief, 4 mg of catalyst and 30 μL of Nafion solution (5 wt%) were dispersed in 1 mL of water/isopropanol solution (3 : 1 v/v) and sonicated for 40 min to form a homogeneous ink. Then, 5 μL of the ink was loaded onto the surface of the GCE and dried at room temperature. The OER and HER performances were both evaluated in N_2-saturated 1.0 M KOH solution, respectively, by using a Ag/AgCl electrode as the reference and a graphite rod as the counter electrode. To examine the electrocatalytic activity of the catalysts, polarization curves were obtained by using linear sweep voltammetry (LSV) with a scan rate of 5 mV s^{-1}. The stability of the electrocatalyst was investigated by a multi-current step test. All catalytic potentials in this work were referenced to a reversible hydrogen electrode (RHE) by the equation:

$$E_{RHE} = E_{Ag/AgCl} + 0.059\ pH + E^0_{Ag/AgCl}\ (E^0_{Ag/AgCl} = 0.197\ V) \quad (3)$$

The turnover frequency (TOF; s^{-1}) for OER was calculated with the following equation:

$$TOF = I/(4Fn) \quad (4)$$

The TOF for HER was calculated with the following equation:

$$TOF = I/(2Fn) \quad (5)$$

where *I* is the current (A), *F* is the Faraday constant (C mol^{-1}), and *n* is the number of active sites (mol). The factors of 1/4 or 1/2 are the corresponding electron transfer numbers.

Results and discussion

The synthesis process for making Fe–$NiCo_2O_4$@HNCP is shown in an overview (Fig. 2a). ZIF-67 was fabricated (Fig. S5†) as a sacrificial template.[29] After an *in situ* polymerization process, a thin layer of polyaniline was uniformly covered on the surface of ZIF-67 (Fig. S6†). The hollow polyaniline polyhedron is generated after removal of the ZIF-67 template by acid etching, as illustrated in Fig. S7.† After a one-step pyrolysis, a hollow N-doped carbon polyhedron (HNCP) was obtained (Fig. 2b and the corresponding XRD pattern is displayed in Fig. S8†), which is regarded as an ideal matrix for further solution co-deposition of iron-doped nickel-cobalt layered double hydroxides (Fe–NiCo LDH) nanosheets (Fig. S9†). Finally, Fe–$NiCo_2O_4$@HNCP (Fig. 2c) was successfully obtained after heat treatment to break

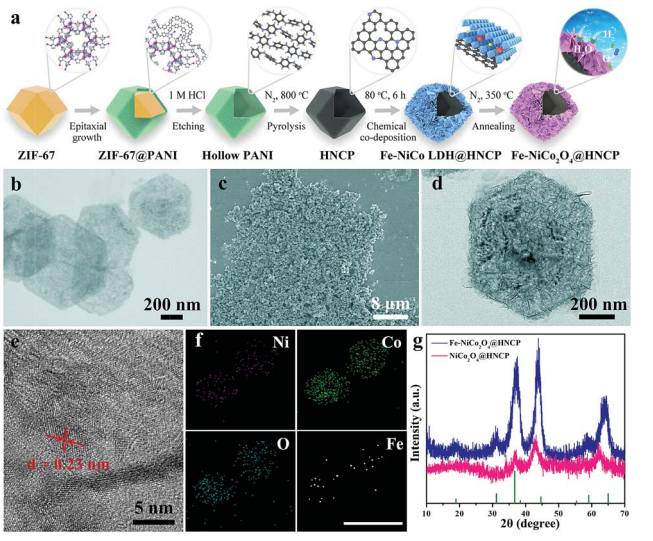

Fig. 2 (a) Schematic illustration of the synthesis process of Fe–$NiCo_2O_4$@HNCP. (b) TEM image of hollow nitrogen-doped carbon polyhedron. (c) SEM, (d) TEM, and (e) HRTEM images of Fe–$NiCo_2O_4$@HNCP. (f) Elemental mappings of Ni, Co, O, and Fe in Fe–$NiCo_2O_4$@HNCP. The bar length is 1 μm. (g) XRD patterns of Fe–$NiCo_2O_4$@HNCP and $NiCo_2O_4$@HNCP.

the hydrotalcite structure. As shown in Fig. 2d, ultrathin Fe–$NiCo_2O_4$ nanosheets with a thickness of ~8.0 nm (Fig. S10†) were anchored on the surface of HNCP to form an integral hollow polyhedron of Fe–$NiCo_2O_4$@HNCP. No large clusters/nanoparticles were observed from the TEM images, which rules out the possibility of forming heterogeneous iron oxide compounds. The HRTEM image of Fe–$NiCo_2O_4$@HNCP (Fig. 2e) reveals fringe spacings of about 0.23 nm, corresponding to the (311) plane of the spinel structured $NiCo_2O_4$, which indicates a negative effect towards its crystalline structure after iron doping. Energy-dispersive X-ray spectroscopy (EDS) elemental mapping images reveal that the Fe element is evenly distributed over the entire Fe–$NiCo_2O_4$@HNCP (Fig. 2f). The X-ray diffraction (XRD) patterns also show no other crystal phases except $NiCo_2O_4$ for both Fe–$NiCo_2O_4$@HNCP and $NiCo_2O_4$@HNCP, proving the uniform Fe doping in the atomic structure of $NiCo_2O_4$ nanosheets. Six peaks, *i.e.* 18.8°, 31.3°, 37.2°, 44.1°, 58.7°, and 64.1°, can be well indexed to the (111), (220), (311), (400), (511), and (440) planes of spinel-structured Fe–$NiCo_2O_4$ and $NiCo_2O_4$ (JCPDS card no. 73-1702).

The pore structure analysis on Fe–$NiCo_2O_4$@HNCP was characterized by nitrogen adsorption–desorption. As shown in Fig. 3a, the Fe–$NiCo_2O_4$@HNCP displays a typical type IV isotherm with a distinct hysteresis loop, which indicates an abundant mesoporous structure (Fig. 3b). The Brunauer–Emmett–Teller (BET) specific surface area and total pore volume of Fe–$NiCo_2O_4$@HNCP are 116 m^2 g^{-1} and 0.2 cm^3 g^{-1}, respectively, with mesopores of diameter mainly concentrated at 33 nm. Compared with the lower specific surface area (8.7 m^2 g^{-1}) and total pore volume (0.026 cm^3 g^{-1}) of bulk Fe–$NiCo_2O_4$, the high porosity of Fe–$NiCo_2O_4$@HNCP is beneficial for electrolyte adsorption and charge transport for electrocatalysis. X-Ray photoelectron spectroscopy (XPS) was used to study the valence states and bonding in Fe–$NiCo_2O_4$@HNCP and $NiCo_2O_4$@HNCP. As shown in Fig. 3c, the peaks at 711.6 eV and 725.4 eV with a peak separation of 13.8 eV in the Fe 2p spectrum, are typical for Fe^{3+} species, further confirming the efficient doping of Fe^{3+} in $NiCo_2O_4$ nansoheets.[30,31] The amount of Fe incorporation in the Fe–$NiCo_2O_4$ nanosheets is calculated as 4.65 atom%. The obvious negative shifts of the binding energies of Co 2p (Fig. 3d) and Ni $2p_{3/2}$ (Fig. 3e) in Fe–$NiCo_2O_4$@HNCP are *ca.* 0.65 eV and 0.56 eV, respectively, compared with those of $NiCo_2O_4$@HNCP. This indicates increased electronic interactions between the Fe and Ni/Co elements, which are caused by the enhanced charge delocalizations in the $NiCo_2O_4$ nanosheets after Fe doping. This enhanced surface electronic property is beneficial for strong interactions between the catalyst and electrolyte, as well as charge mobility during electrocatalysis. The N 1s spectrum (Fig. 3f) displays three peaks corresponding to N-6 (pyridine-like nitrogen atom) at 399.2 eV, N-5 (pyrrolic-like nitrogen atom) at 399.7 eV, and N-Q (quaternary nitrogen atom) at 400.3 eV. The nitrogen atoms in the outer layer of the hollow nitrogen-doped carbon polyhedron is beneficial for bonding Fe–$NiCo_2O_4$ nanosheets and maintaining structural integrity. Meanwhile, the highly active nitrogen atoms on the inner wall of HNCP can contact the electrolyte directly, to split water into hydrogen and oxygen efficiently.

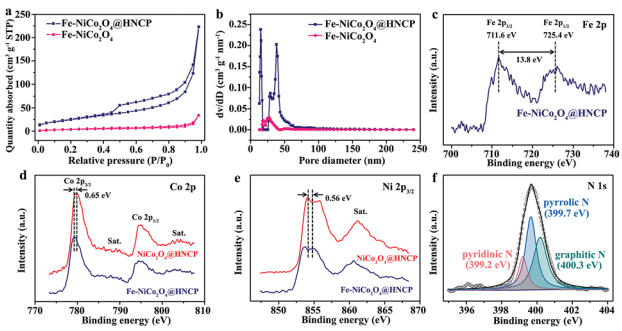

Fig. 3 (a) N_2 adsorption–desorption isotherms, and (b) the corresponding pore size distribution plots of Fe–$NiCo_2O_4$@HNCP and Fe–$NiCo_2O_4$. (c) Fe 2p spectrum of Fe–$NiCo_2O_4$@HNCP. (d) Co 2p, and (e) Ni 2p spectra of Fe–$NiCo_2O_4$@HNCP and $NiCo_2O_4$@HNCP, respectively. (f) N 1s spectrum of Fe–$NiCo_2O_4$@HNCP.

To illustrate the role that transition-metal doping plays in the OER and HER processes, the fabricated Fe–$NiCo_2O_4$@HNCP, $NiCo_2O_4$@HNCP, and pristine $NiCo_2O_4$ catalysts were tested in a three-electrode electrochemical cell in a 1.0 M KOH solution. Fig. 4a shows the polarization curves of all the samples. This clearly shows the better OER activity of Fe–$NiCo_2O_4$@HNCP with a lower overpotential (η) of 0.27 V than those of $NiCo_2O_4$@HNCP ($\eta = 0.34$ V) and pristine $NiCo_2O_4$ ($\eta =$ 0.38 V). The overpotential required to drive a high current density of 10 mA cm^{-2} is 0.30 V for Fe–$NiCo_2O_4$@HNCP, which is also the smallest value among the four samples shown in Fig. 4a. The turnover frequency (TOF) value of Fe–$NiCo_2O_4$@HNCP is calculated to be 0.0883 s^{-1} at the overpotential of

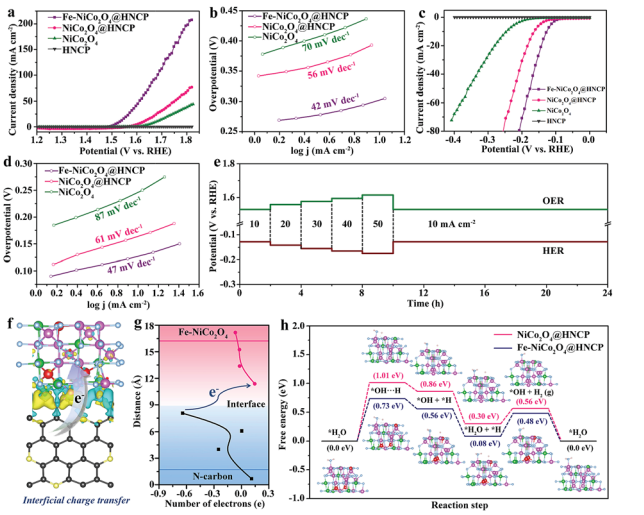

Fig. 4 (a) Polarization curves, and (b) Tafel curves of Fe–$NiCo_2O_4$@HNCP and the compared samples in 1.0 M KOH solution for OER with a scan rate of 5 mV s^{-1}. (c) Polarization curves, and (d) Tafel curves of Fe–$NiCo_2O_4$@HNCP and the compared samples in 1.0 M KOH solution for HER with a scan rate of 5 mV s^{-1}. (e) Stability tests of Fe–$NiCo_2O_4$@HNCP at varied current densities for both OER and HER processes. (f) Charge density distribution of Fe–$NiCo_2O_4$@HNCP around the interface. (g) Bader charge analysis of average atoms near the interface of N-carbon and Fe–$NiCo_2O_4$. (h) Calculated free energy diagram of the HER on Fe–$NiCo_2O_4$, and $NiCo_2O_4$.

350 mV (Fig. S12a†), which is 16.4 and 58.9 times higher than those of $NiCo_2O_4$@HNCP (0.0054 s^{-1}) and pristine $NiCo_2O_4$ (0.0015 s^{-1}), respectively. Furthermore, the linear portions of the Tafel plots (Fig. 4b) were fitted to the Tafel equation ($\eta = a + b \log j$, where j and b are current density and Tafel slope, respectively), revealing that the Fe–$NiCo_2O_4$@HNCP possesses a smaller Tafel slope (42 mV dec^{-1}) than $NiCo_2O_4$@HNCP (56 mV dec^{-1}) and pristine $NiCo_2O_4$ (70 mV dec^{-1}). This indicates more rapid OER rates for Fe–$NiCo_2O_4$@HNCP. The overpotential and Tafel slope of Fe–$NiCo_2O_4$@HNCP are also favorable compared to most recently reported earth-abundant OER electrocatalysts (Table S2†). We hypothesize that the Fe doping and hollow N-doped carbon polyhedron play crucial roles in improving the electrocatalytic activity of $NiCo_2O_4$ toward OER. This could be attributed to the fact that proper Fe doping is beneficial to modulating the energy level of $NiCo_2O_4$ with a partially delocalized charge.[32,33] Meanwhile, the favorable connection between highly conductive HNCP and $NiCo_2O_4$ can also boost its interfacial electronic conductivity. Attributing to the above-mentioned thermodynamic and kinetic superiority, we also investigated the HER performance of Fe–$NiCo_2O_4$@HNCP in 1.0 M KOH solution. As the polarization curves shown in Fig. 4c, Fe–$NiCo_2O_4$@HNCP exhibits small overpotentials of 84 mV and 124 mV at current densities of 1 and 10 mA cm^{-2}, respectively. Meanwhile, the TOF value of Fe–$NiCo_2O_4$@HNCP is calculated to be 0.39 s^{-1} at an overpotential of 200 mV (Fig. S12b†). The excellent HER activity of Fe–$NiCo_2O_4$@HNCP is further proved by its low Tafel slop. Generally, there are three possible pathways involving the HER process in alkaline media, referred to as the Volmer, Heyrovsky, and Tafel reactions.[34,35]

$$H_2O + e^- \rightarrow H_{ads} + OH^- \text{ (Volmer, } b \approx 120 \text{ mV dec}^{-1}) \quad (6)$$

$$H_{ads} + H_2O + e^- \rightarrow H_2 + OH^- \text{ (Heyrovsky, } b \approx 40 \text{ mV dec}^{-1}) \quad (7)$$

$$H_{ads} + H_{ads} \rightarrow H_2 \text{ (Tafel, } b \approx 30 \text{ mV dec}^{-1}) \quad (8)$$

Depending upon the rate-limiting step, the above three pathways can be separated into two mechanisms (Volmer–Heyrovsky and Volmer–Tafel). As shown in Fig. 4d, the Tafel value of Fe–$NiCo_2O_4$@HNCP is 47 mV dec^{-1}, which demonstrates it proceeded *via* a Volmer–Heyrovsky mechanism. The HER performance of Fe–$NiCo_2O_4$@HNCP is much more outstanding than that of most of Ni(Co)-based electrocatalysts (Table S3†), even approaching that of metal phosphides (such as NiCoP,[36] CoPS,[37] and CoP[38]) in an acidic electrolyte. To value the stability of the Fe–$NiCo_2O_4$@HNCP, a series of current densities (10, 20, 30, 40, and 50 mA cm^{-2}) were sequentially carried out for 10 h for both OER and HER (Fig. 4e). Fe–$NiCo_2O_4$@HNCP exhibits a superior durability with the overpotential, showing almost no change under various current densities. Furthermore, the overpotential renews rapidly after reverting the current density from the high value of 50 to 10 mA cm^{-2}, and prevails over an additional 14 h test. This indicates the excellent stability of Fe–$NiCo_2O_4$@HNCP for water splitting under high current densities.

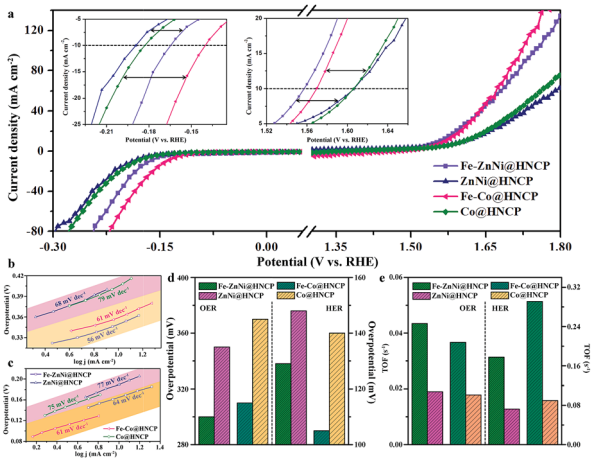

Fig. 5 (a) Polarization curves of the Fe-doped spinel-structured nanosheet@HNCP for both the oxygen evolution reaction and the hydrogen evolution reaction. Inset: enlargement of the region near the onset. The related Tafel plots for (b) OER, and (c) HER, respectively. (d) Comparison of overpotentials of various samples at a current density of 1 mA cm^{-2} for both OER and HER. (e) Comparison of TOF values of various samples for OER at η = 350 mV, and HER at η = 200 mV, respectively.

For further insights into the excellent water splitting ability of Fe–$NiCo_2O_4$@HNCP, DFT calculations were applied to illustrate the unique synergistic structure–property relationship between the electronic structure and rich active sites *via* the perspectives of thermodynamic and kinetic acceleration. From the thermodynamic view, the energy level of pristine $NiCo_2O_4$ can be tuned properly by transition-metal doping engineering (especially, Fe doping) as mentioned in Fig. 1, leading to a much lower applied overpotential/energy for water splitting. Meanwhile, the delocalized charge in Fe–$NiCo_2O_4$ makes it a "charge-rich" phase to boost the electrocatalytic property. To go further, the model of Fe–$NiCo_2O_4$@HNCP is built by aligning optimized Fe–$NiCo_2O_4$ with highly conductive nitrogen-doped carbon (Fig. 4f and S14†). As shown in Fig. 4g, the charge density difference indicates that the electrons transfer from the nitrogen-doped carbon support to the partially charge-delocalized Fe–$NiCo_2O_4$ component, making the d-orbital of Ni/Co/Fe cations increase the electronic states around the Fermi level. As previously reported, the enriched d-orbital electrons are significant for the acceleration towards the hydrogen evolution reaction.[39] As a result, the increased electronic states induced by the HNCP lead to an enhanced HER performance by increasing the binding strength between catalyst and H. Secondly, from the perspective of kinetic acceleration, the Fe–$NiCo_2O_4$ nanosheets are anchored on the surface of a hollow nitrogen-doped carbon polyhedron, which provides a higher specific surface area with more active sites for electrolyte adsorption compared with the aggregated $NiCo_2O_4$ bulk. Meanwhile, the charge delocalization around the Ni/Co/Fe cations can increase the effective active area, which is equivalent to increasing the number of active sites of Fe–$NiCo_2O_4$@HNCP after Fe doping. As demonstrated by the Gibbs free energy diagrams (Fig. 4h), the energy barrier (ΔG) of Fe–

$NiCo_2O_4$@HNCP for HER is much lower than that of $NiCo_2O_4$@HNCP, which includes four intermediate states: (1) adsorption of H_2O (*H_2O, ΔG_1); (2) dissociation of water to form adsorbed H and OH (*OH + *H, ΔG_2); (3) structural adjustment after getting an H atom to form adsorbed H_2O and H (*H_2O + *H, ΔG_3); (4) combination of *H with a proton from an adjacent *H_2O to generate adsorbed OH and H_2 (g) (*OH + H_2 (g), ΔG_4). Detailed investigations on the Gibbs free energies reveal that the Fe–$NiCo_2O_4$@HNCP shows the optimal level for an H adsorption step with lower $\Delta G_2 = 0.56$ eV and activation energy (AE) of 0.73 eV, compared with those of $NiCo_2O_4$@HNCP ($\Delta G_2 =$ 0.86 eV, AE = 1.01 eV). The calculated ΔG_2 values can be correlated with their electronic structures, which can reveal the origin of their reactivity *via* the d-band center theory (Fig. S15†).[40] Generally, a catalyst with a low d-band position (such as $NiCo_2O_4$ in this case, $\varepsilon_{d,1} = -1.15$ eV), has a weak H adsorption; however, for the catalyst with a high d-band position (such as Fe–$NiCo_2O_4$ in this case, $\varepsilon_{d,2} = -1.02$ eV), the hydrogen bonding is strong for a lower value of ΔG_2. As mentioned above, this strong H chemisorption of the Ni(Co)–Ni(Co) bridge is beneficial to improving the HER performance. To our knowledge, the positive shift of the d-band center of Fe–$NiCo_2O_4$ is caused by the partially delocalized charge from Fe atom to the adjacent Ni/Co atom, which has been correlated with the XPS results as negatively shifted binding energies of Co 2p and Ni $2p_{3/2}$ (Fig. 3d and e). In spite of a slightly higher energy barrier of H_2 desorption for Fe–$NiCo_2O_4$@HNCP ($\Delta G_4 =$ 0.40 eV) than that of 0.26 eV for $NiCo_2O_4$@HNCP, this chemisorption is not a rate-determining step during the whole HER processes. Therefore, it is an efficient strategy to boost the water splitting ability of $NiCo_2O_4$ nanosheets by the combination of transition-metal doping engineering and hollow heteroatom-doping carbon shell construction from both the thermodynamic and kinetic viewpoints.

To further confirm the positive effect of the transition-metal doping engineering on the water splitting process, various other transition-metals, such as Cu, Mn, and Zn, were applied to replace Fe for synthesizing Cu–$NiCo_2O_4$@HNCP, Mn–$NiCo_2O_4$@HNCP, and Zn–$NiCo_2O_4$@HNCP. Their structures are reported in the ESI (Fig. S16–S18†). Obvious negative shifts for the binding energies of both Co and Ni elements were observed (Fig. S18d and e†), mainly originating from the partially delocalized charge from the transition metals (Cu, Mn, and Zn) to Ni/Co elements (Fig. S2–S4†). As a result, TM-$NiCo_2O_4$@HNCP catalysts showed lower overpotentials and smaller Tafel slopes than the corresponding $NiCo_2O_4$@HNCP, demonstrating the important role of transition-metals in the water splitting process (Fig. S19†).

Furthermore, the successful manipulation of the water splitting activity of TM-$NiCo_2O_4$@HNCP inspires us to reveal the positive effect of transition-metal doping engineering towards other spinel-structured nanosheets. Therefore, by taking Fe as an example of a transition metal, all the samples doped with Fe show lower overpotentials, higher current densities, smaller Tafel slopes and larger TOF values for both OER and HER, than the corresponding catalysts without transition-metal doping (Fig. 5). These results demonstrate the positive role of transition-metal doping engineering for spinel-structured nanosheets in the water splitting process, as a result of the partially delocalized charge in the spinel-structured nanosheets.

Conclusions and outlook

In summary, we have uncovered that transition-metal doping engineering is an efficient method to promote the electrocatalytic performance of spinel-structured nanosheets. Our results demonstrate that partially delocalized charges on both the Fe–$NiCo_2O_4$ surface and the interface between the Fe–$NiCo_2O_4$ and HNCP support can significantly boost the water splitting performance. Taking Fe–$NiCo_2O_4$@HNCP as a model system, the fundamental synergistic relationship between electronic structure and rich active sites is clearly revealed *via* the perspectives of thermodynamic and kinetic acceleration during the electrocatalytic process, by combination of experimental analysis and DFT calculation. Fe–$NiCo_2O_4$@HNCP exhibits low overpotentials and small Tafel slopes of $\eta = 270$ mV and $b = 42$ mV dec^{-1} for the OER, and $\eta = 84$ mV and $b =$ 47 mV dec^{-1} for the HER, respectively, as well as robust stability, implying its superiority as a bifunctional electrocatalyst. Furthermore, the rule of transition-metal doping engineering can also be applied to other spinel-structured nanosheets. Therefore, this work demonstrates that energy level control with a partially delocalized charge *via* transition-metal doping accounts for the promoted water splitting process from both experimental and theoretical points of view, which provides guidelines for the future design of electrocatalysts.

Conflicts of interest

There are no conflicts to declare.

Acknowledgements

We are really grateful for the financial support from the National Natural Science Foundation of China (51433001, 21674019, 21604010), the Science and Technology Commission of Shanghai Municipality (16520722100), the Program of Shanghai Academic Research Leader (17XD1400100), the "Chenguang Program" supported by the Shanghai Education Development Foundation and Shanghai Municipal Education Commission (16CG39) and the Engineering and Physical Sciences Research Council (EPSRC, EP/L015862/1). The computational center of USTC is acknowledged for computational support.

References

1 M. D. Symes and L. Cronin, *Nat. Chem.*, 2013, **5**, 403–409.
2 T. Y. Ma, S. Dai and S. Z. Qiao, *Mater. Today*, 2016, **19**, 265–273.
3 Y. F. Yu, Y. M. Shi and B. Zhang, *Acc. Chem. Res.*, 2018, **51**, 1711–1721.

4 C. H. Choi, K. Chung, T. T. H. Nguyen and D. H. Kim, *ACS Energy Lett.*, 2018, **3**, 1415–1433.
5 J. T. Zhang, L. T. Qu, G. Q. Shi, J. Y. Liu, J. F. Chen and L. M. Dai, *Angew. Chem., Int. Ed.*, 2016, **55**, 2230–2234.
6 Y. Zheng, Y. Jiao, Y. H. Zhu, Q. R. Cai, A. Vasileff, L. H. Li, Y. Han, Y. Chen and S. Z. Qiao, *J. Am. Chem. Soc.*, 2017, **139**, 3336–3339.
7 Z. J. Wang, Y. Z. Lu, Y. Yan, T. Y. P. Larissa, X. Zhang, D. Wu, H. Zhang, Y. H. Yang and X. Wang, *Nano Energy*, 2016, **30**, 368–378.
8 F. L. Lai, D. Y. Yong, X. L. Ning, B. C. Pan, Y. E. Miao and T. X. Liu, *Small*, 2017, **13**, 1602866.
9 Y. E. Miao, F. Li, Y. Zhou, F. L. Lai, H. Y. Lu and T. X. Liu, *Nanoscale*, 2017, **9**, 16313–16320.
10 Y. F. Sun, S. Gao, F. C. Lei, J. W. Liu, L. Liang and Y. Xie, *Chem. Sci.*, 2014, **5**, 3976–3982.
11 J. K. Norskov, T. Bligaard, A. Logadottir, J. R. Kitchin, J. G. Chen, S. Pandelov and J. K. Norskov, *J. Electrochem. Soc.*, 2005, **152**, J23–J26.
12 T. Ling, D. Y. Yan, Y. Jiao, H. Wang, Y. Zheng, X. L. Zheng, J. Mao, X. W. Du, Z. P. Hu, M. Jaroniec and S. Z. Qiao, *Nat. Commun.*, 2016, **7**, 12876.
13 Z. F. Huang, J. Wang, Y. C. Peng, C. Y. Jung, A. Fisher and X. Wang, *Adv. Energy Mater.*, 2017, **7**, 1700544.
14 D. W. Ding, B. T. Dong, J. Liang, H. Zhou, Y. C. Pang and S. J. Ding, *ACS Appl. Mater. Interfaces*, 2016, **8**, 24573–24578.
15 J. Xu, X. Xiao, J. Zhang, J. J. Liu, J. K. Ni, H. G. Xue and H. Pang, *Part. Part. Syst. Char.*, 2017, **34**, 1600420.
16 H. Hu, B. Y. Guan, B. Y. Xia and X. W. Lou, *J. Am. Chem. Soc.*, 2017, **137**, 5590–5595.
17 X. H. Gao, H. X. Zhang, Q. G. Li, X. G. Yu, Z. L. Hong, X. W. Zhang, C. D. Liang and Z. Lin, *Angew. Chem., Int. Ed.*, 2016, **55**, 6290–6294.
18 T. Ling, D. Y. Yan, H. Wang, Y. Jiao, Z. P. Hu, Y. Zheng, L. R. Zheng, J. Mao, H. Liu, X. W. Du, M. Jaroniec and S. Z. Qiao, *Nat. Commun.*, 2017, **8**, 1509.
19 J. Bao, X. D. Zhang, B. Fan, J. J. Zhang, M. Zhou, W. L. Yang, X. Hu, H. Wang, B. C. Pan and Y. Xie, *Angew. Chem., Int. Ed.*, 2015, **54**, 7399–7404.
20 Y. Shi, Y. Zhou, D. R. Yang, W. X. Xu, C. Wang, F. B. Wang, J. J. Xu, X. H. Xia and H. Y. Chen, *J. Am. Chem. Soc.*, 2017, **139**, 15479–15485.
21 V. Augustyn, S. Therese, T. C. Turner and A. Manthiram, *J. Mater. Chem. A*, 2015, **3**, 16604–16612.
22 P. E. Blochl, *Phys. Rev. B: Condens. Matter Mater. Phys.*, 1994, **50**, 17953–17979.
23 J. P. Perdew, K. Burke and M. Ernzerhof, *Phys. Rev. Lett.*, 1996, **77**, 3865–3868.
24 H. J. Monkhorst and J. D. Pack, *Phys. Rev. B: Condens. Matter Mater. Phys.*, 1976, **13**, 5188–5192.
25 B. E. Conway and B. V. Tilak, *Electrochim. Acta*, 2002, **47**, 3571–3594.
26 G. Henkelman, B. P. Uberuaga and H. Jonsson, *J. Chem. Phys.*, 2000, **113**, 9901–9904.
27 F. L. Lai, Y. E. Miao, Y. P. Huang, Y. F. Zhang and T. X. Liu, *ACS Appl. Mater. Interfaces*, 2016, **8**, 3558–3566.
28 X. B. Zhu, L. L. Mo, Y. Wu, F. L. Lai, X. M. Han, X. Y. Ling, T. X. Liu and Y. E. Miao, *Compos. Commun.*, 2018, **9**, 86–91.
29 R. B. Wu, D. P. Wang, X. H. Rui, B. Liu, K. Zhou, A. W. K. Law, Q. Y. Yan, J. Wei and Z. Chen, *Adv. Mater.*, 2015, **27**, 3038–3044.
30 Y. Jia, L. Zhang, G. Gao, H. Chen, B. Wang, J. Zhou, M. Soo, M. Hong, X. Yan, G. Qian, J. Zou, A. Du and X. D. Yao, *Adv. Mater.*, 2017, **29**, 1700017.
31 S. H. Ye, Z. X. Shi, J. X. Feng, Y. X. Tong and G. R. Li, *Angew. Chem., Int. Ed.*, 2018, **57**, 2672–2676.
32 Y. J. Li, H. C. Zhang, M. Jiang, Q. Zhang, P. L. He and X. M. Sun, *Adv. Funct. Mater.*, 2017, **27**, 1702513.
33 X. D. Jia, Y. F. Zhao, G. B. Chen, L. Shang, R. Shi, X. F. Kang, G. Waterhouse, L. Z. Wu, C. H. Tung and T. R. Zhang, *Adv. Energy Mater.*, 2016, **6**, 1502585.
34 G. Zhang, Y. S. Feng, W. T. Lu, D. He, C. Y. Wang, Y. K. Li, X. Y. Wang and F. F. Cao, *ACS Catal.*, 2018, **8**, 5431–5441.
35 Q. Q. Zhou, T. T. Li, J. J. Qian, Y. Hu, F. Y. Guo and Y. Q. Zheng, *J. Mater. Chem. A*, 2018, **6**, 14431–14439.
36 C. Du, L. Yang, F. L. Yang, G. Z. Cheng and W. Luo, *ACS Catal.*, 2017, **7**, 4131–4137.
37 M. Caban-Acevedo, M. L. Stone, J. R. Schmidt, J. G. Thomas, Q. Ding, H. C. Chang, M. L. Tsai, J. H. He and S. Jin, *Nat. Mater.*, 2015, **14**, 1245–1251.
38 J. W. Ma, M. Wang, G. Y. Lei, G. L. Zhang, F. B. Zhang, W. C. Peng, X. B. Fan and Y. Li, *Small*, 2018, **14**, 1702895.
39 C. Tang, L. F. Gan, R. Zhang, W. B. Lu, X. E. Jiang, A. M. Asir, X. P. Sun, J. Wang and L. Chen, *Nano Lett.*, 2016, **16**, 6617–6621.
40 Y. Zheng, Y. Jiao, Y. H. Zhu, L. H. Li, Y. Han, Y. Chen, M. Jaroniec and S. Z. Qiao, *J. Am. Chem. Soc.*, 2016, **138**, 16174–16181.